Journal of Applied Fluid Mechanics, Vol. 17, No. 5, pp. 1039-1051, 2024.
Available online at www.jafmonline.net, ISSN 1735-3572, EISSN 1735-3645.
https://doi.org/10.47176/jafm.17.05.2270

Investigation of Distribution Characteristics of Cylindrical Particles after the Rupture of Modular Cartridges in a Simulator Chamber

Z. Y. Li, Y. G. Yu† and A. Chen

School of Energy and Power Engineering, Nanjing University of Science and Technology, Nanjing, Jiangsu Province, 210094, China

†*Corresponding Author Email: 801105ndd@njust.edu.cn*

ABSTRACT

Modular charging is an advanced technique designed to meet the requirements of auto-loading artillery, whereby granular propellants are stored within modular cartridges that are loaded into the gun chamber. This study employed an extended coupled computational fluid dynamics-discrete element method (CFD-DEM) approach to investigate the gas-particle flow within modular charges. After model validation, we analyzed the distribution characteristics, velocity, coordination number, and orientation of cylindrical pellets in a simulator chamber. Four different loading positions for modular cartridges were examined to assess their impact on particle distribution. Numerical simulations revealed a combination of gentle, horizontal, and steep slopes in the particle distribution. The maximum particle velocity experienced a rapid increase during the initial phase, followed by a zigzag decline after reaching its peak. High-coordination number particles tended to accumulate primarily in the middle layer of steep accumulation. Additionally, the particles exhibited an inverted V-shape orientation range from 0° to 180°, suggesting their tendency to assume upright positions. This established model significantly enhanced our understanding of particle distribution following module cartridge rupture and provided valuable guidance for optimizing the design of large-caliber artillery charges.

Article History

Received August 29, 2023
Revised December 20, 2023
Accepted December 23, 2023
Available online February 24, 2024

Keywords:

Gas-solid flow
CFD-DEM method
Multi-sphere model
Cylindrical particles
Particle distribution

1. INTRODUCTION

Particulate matter is commonly encountered in both natural and engineering contexts, and accurately measuring its mechanical behavior and mobility through experimentation can be challenging. Granular propellants, a specific type of granular material, are packed into modular containers to create the granular propellant charge bed. Indeed, understanding the gas-particle flow within the chamber during the early stages of interior ballistics is crucial but complex to predict. It has been established that the formation of initial reverse differential pressure, which can impact the stability of the gun's interior ballistics and even lead to safety incidents such as chamber explosions, is primarily attributed to the uneven distribution of propellant grains caused by compressing the propellant bed (Sheu & Lee, 1995). Therefore, it is essential to conduct detailed simulations of the gas-particle flow within the chamber of modular charges to optimize charging, design, and ignition procedures.

In recent decades, numerous studies have attempted to address two-phase flow problems in interior ballistics using various numerical models, including the lumped parameter model (Zhao, 2003; Lu et al., 1999), the one-dimensional two-phase model (Lu et al., 1999), and the multi-dimensional two-phase model (Briand et al., 1992; Lu & Zhou, 1999; 2001). The application of numerical methods is a cost-effective alternative to physical experimentation, enabling the acquisition of data that is challenging to measure experimentally. However, these methods treat gas and particle phases as interpenetrating continuous media, ignoring interactions between particles and collisions with walls. Consequently, they fail to provide accurate information on the intricate dynamics of particle-scale gas-solid flows. The Discrete Element Method (DEM) is extensively used in studying the behavior of assemblies of real particles, enabling an accurate representation of individual particle characteristics and interactions. Initially employed by Cundall and Strack (1979) in the investigation of rock and soil mechanics, the soft-sphere DEM is increasingly being adopted in particle packing studies (Nan et al., 2014; Soltanbeigi et al., 2018; Zhao et al., 2018) and particle flow simulations (Höhner et al., 2012; Ma & Zhao, 2018b; Gao et al., 2022), owing to advancements in computing

NOMENCLATURE

c_1, c_2, c_3,c_4	fitted constants in Eq. (1)	s	surface areas of sphere with equivalent spherical diameter of particle
C_d	drag coefficient	T_p	total torque exerted on particle
F_c	contact force	u_g	velocity vector of gas
$F_{d,i}$	drag force for particle i	v_p	translational velocity of particle
F_{pf}	particle/fluid force	V_c	volume of computational cells
G_p	gravitational force of particle	α	steep slope accumulation angle
g	gravitational acceleration	ε_g	volume fraction of gas
h	height of particle accumulation in y=0	θ	nutation angle/Orientation angle
I_p	inertia moment of particle	ψ	precession angle
L	distance between Module 1 and the breech end	φ	spin angle
L_p	axial length of steep slope accumulation	φ	sphericity
L_h	axial length of horizontal slope accumulation	ρ_g	density of gas
m_p	particle mass	τ_g	viscous stress tensor of gas
Re_{sph}	Reynolds number based on equivalent spherical diameter of particle,	ω_p	rotational velocity of particle
S_p	momentum exchange between gas and particle	∇p	fluid pressure gradient
S	actual surface area of the particle		

power. When using non-spherical DEM simulations, several relevant published works have demonstrated the critical role of particle shape in determining the morphology and structure of particle accumulation, significantly impacting the discharge rate and particle mixing (Tao et al., 2010; Ma & Zhao, 2018a; Zhao et al., 2018).

CFD simulations have emerged as a powerful tool for investigating and optimizing fluid dynamics in various fields, including fluidized beds (Liu et al., 2015; Nan et al., 2016), micro heat exchangers (Manda et al., 2020; Manda & Mazumdar, 2023a), the blast furnace raceway (Wei et al., 2019), and agricultural seeding (Lei et al., 2018). The extensive use of the CFD technique is primarily attributed to their efficacy in addressing complex fluid phenomena, particularly in turbulent flows featuring heat and mass transfer (Wei et al., 2019; Manda et al., 2022, 2023). The combination of CFD and DEM in numerical models is extensively utilized for studying particle-fluid flow systems, establishing itself as one of the most prevalent numerical methodologies. In contrast to particle packing and particle flows, gas-solid flow systems with non-spherical particles inherently exhibit greater complexity. The coupled CFD-DEM approach was initially presented by Tsuji et al. (1992) for investigating dense gas-solid flow in pneumatic conveyors and was subsequently employed to model the two-dimensional fluidized bed. In past fewer years, there has been a growing number of scholars developing and improving the method, investigating the dynamics of non-spherical particles in spouted fluidized beds (Atxutegi et al., 2021; Zhou et al., 2022), pneumatic conveying (Oschmann et al., 2015) and bubbling fluidized beds (Wang et al., 2016; Li et al., 2022) The influence of different particle shapes, such as spherical, cylindrical, rod-shaped, and irregularly shaped particles, on particle motion characteristics in various fluidized bed systems and conveying processes were numerically investigated using CFD-DEM in the current study (Shao et al., 2014; Ren et al., 2014; Chen et al., 2022). Additionally, the characteristics of gas-solid flow, including bubble shape, fluidization properties, and flow behavior, are influenced by particle size (Wang et al., 2021).

Despite its capability to precisely consider gunpowder particles' size and shape while providing an extensive representation of interactions between particles as well as with walls, there is limited usage of DEM in analyzing gas-solid two-phase flow within propellant beds, particularly for modular charges. Instead, the Euler-Euler system is used to define gas and particle phases as interpenetrating continuous media in the two-fluid model, which is frequently employed for studying the gas-solid flow in a gun system's internal ballistic process (Zhang & Yuan, 2016). Cheng and Zhang (2013) took the lead in using the CFD-DEM to describe the central point fire transfer of granular propellant on a particle scale by developing a two-dimensional two-phase fluid-structure coupling model. Then, utilizing experimental data and numerical simulations, Chen and Yu (2022, 2023) developed a three-dimensional unsteady gas-solid two-phase flow model based on the CFD-DEM method. This model predicted the impact of module-primer distance in single-module charge and double-module charge on particle dispersion morphology during ignition. These studies, however, ignore the impact of particle shape on dynamic performance and treat gunpowder particles as spherical despite though the majority of the granular gunpowder is not spherical, such as cylindrical.

Here, a numerical investigation was conducted using the three-dimensional CFD-DEM approach to examine the particle motion behavior and distribution subsequent to module cartridge rupture during ignition process of modular charges. The distribution and behavioral characteristics of cylindroid propellant pellets were discussed and analyzed under varying initial particle bed structures, providing a foundation for comprehending the modular charge's particle distribution during the ignition process in multiple modules, thereby addressing localized pressure rise caused by uneven powder particle

distribution and optimizing charge design further for large caliber guns.

2. MATHEMATICAL MODEL

2.1 Fluid Motion Model

The continuous equation:

$$\frac{\partial\left(\varepsilon_{\mathrm{g}}\rho_{\mathrm{g}}\right)}{\partial t}+\nabla\cdot\left(\varepsilon_{\mathrm{g}}\rho_{\mathrm{g}}\vec{u}_{\mathrm{g}}\right)=0 \tag{1}$$

The momentum conservation equation:

$$\frac{\partial\left(\varepsilon_{\mathrm{g}}\rho_{\mathrm{g}}\vec{u}_{\mathrm{g}}\right)}{\partial t}+\nabla\cdot\left(\varepsilon_{\mathrm{g}}\rho_{\mathrm{g}}\vec{u}_{\mathrm{g}}\vec{u}_{\mathrm{g}}\right)=-\varepsilon_{\mathrm{g}}\nabla p+\nabla\cdot\left(\varepsilon_{\mathrm{g}}\tau_{\mathrm{g}}\right)+\varepsilon_{\mathrm{g}}\rho_{\mathrm{g}}\vec{g}-\vec{S}_{\mathrm{p}} \tag{2}$$

where u_{g} is the gas velocity vector, g is the gravitational acceleration, and S_{p} is the momentum exchange between gas and particle phases that can be described using the following equation. ε_{g}, ρ_{g}, p_{g} and τ_{g} are the volume fraction, density, pressure and stress tensor of the gas phase, respectively (Norouzi et al., 2016).

$$\vec{S}_{\mathrm{p}}=\frac{1}{V_{\mathrm{c}}}\sum_{i=1}^{n_i}\vec{F}_{\mathrm{d},i} \tag{3}$$

where V_{c} represents the volume of computational cells, n_i denotes the number of particles within a computational cell, and $\vec{F}_{\mathrm{d},i}$ signifies the drag force for particle i.

$$\vec{F}_{\mathrm{d},i}=0.5C_{\mathrm{d}}\rho_{\mathrm{g}}s(\vec{u}_{\mathrm{g}}-\vec{u}_{\mathrm{p}})\left|\vec{u}_{\mathrm{g}}-\vec{u}_{\mathrm{p}}\right| \tag{4}$$

where $\vec{u}_{\mathrm{p}}$ is the velocity of the particle, s is the equivalent spherical surface areas, and C_{d} is the drag coefficient.

Numerous methods have been developed for calculating the drag coefficient C_{d} for non-spherical particles. Among these, the most widely employed approach involves investigating particle shape's effects through the idea of sphericity ϕ. The correlations put forth by Haider and Levenspiel (1989) were chosen for this work.

$$C_{\mathrm{d}}=\frac{24}{\mathrm{Re}_{sph}}\left(1+c_1\,\mathrm{Re}_{sph}{}^{c_2}\right)+\frac{c_3\,\mathrm{Re}_{sph}}{c_4+\mathrm{Re}_{sph}} \tag{5}$$

$$\begin{cases}c_1=\exp\left(2.3288-6.4581\phi+2.4486\phi^2\right)\\ c_2=0.0964+0.5565\phi\\ c_3=\exp\left(4.905-13.8944\phi+18.4222\phi^2-10\phi^3\right)\\ c_4=\exp\left(1.4681+12.2584\phi-20.7322\phi^2+15.8855\phi^3\right)\end{cases} \tag{6}$$

where Re_{sph} is the Reynolds number based on the equivalent spherical area of the non-spherical particle, $\phi=s/S$ is the sphericity, and S denotes the particle's actual surface area. The drag force model can be further enhanced by further investigations because sphericity fails to adequately account for the impact of particle orientation on drag coefficient.

2.2 Particle Motion Model

The interphase forces between the particles and the gas typically include the drag force, Saffman lift force, Magnus force, Basset force and so on. Because of the much higher density of cylindrical particles than gas flow, we only take into account drag, contact, and gravitational forces for this investigation. The Hertz-Mindlin no-slip model, which has the advantage of precise and efficient force calculation, is utilized for computing the contact forces exerted on the spherical elements (Hertz, 1882). Hertzian contact theory is employed to calculate the components of normal force. (Mindlin, 1949). The research of Mindlin and Deresiewicz (1953) served as the foundation for the tangential force components. The movement of a single cylindrical particle can be simplified into two components using Newton's second law: translation and rotation, which can be described as

$$m_{\mathrm{p}}\frac{\mathrm{d}\vec{v}_{\mathrm{p}}}{\mathrm{d}t}=\vec{G}_{\mathrm{p}}+\vec{F}_{\mathrm{c}}+\vec{F}_{\mathrm{pf}} \tag{7}$$

$$\frac{d(\vec{I}_p\,.\,\vec{\omega}_p)}{dt}=\vec{T}_p \tag{8}$$

where m_{p}, G_{p}, F_{c} and F_{pf} are the mass, gravitational force, contact force, particle/fluid force, respectively, v_{p} and ω_{p} represented the translational and rotational velocities, I_{p} is the inertia moment, T_{p} is the total contact torque about its center of mass.

3. PHYSICAL MODELS

3.1 Particle Shape Model

Various approaches, including the super-ellipsoid-based particle model, the multi-sphere model, the bonded-sphere model, and the polyhedron-based model, have been proposed for creating non-spherical particles. In this study, each module was filled with simulated cylindrical pellets and a few real granular propellants. Because the real propellant grains are smaller in volume and quantity than the simulated cylindrical pellets, they were ignored in the simulation. In the simulation experiment, standard cylindrical particles measuring 8 mm in diameter and 13 mm in height were utilized. The numerical simulation employed a multi-sphere model wherein three spherical units with an 8 mm diameter were combined to form cylindroid particles, as illustrated in Fig. 1.

3.2 Geometric Model

The simulator chamber's initial configuration is depicted in Fig. 2(b), which includes two modules, namely Module 1 and Module 2. The distance between the two modules measures 50 mm, while the distance between Module 1 and the breech face amounts to 60 mm. It is worth noting that, for the sake of computational simplicity, the gap between the modular cartridge and the cylindrical tube has been disregarded. Therefore, both the two modules and the tube have a diameter of 135 mm, without considering any movement of the module cartridge within the chamber. Each modular cartridge measures 100 mm in length, while the overall chamber length of the system is

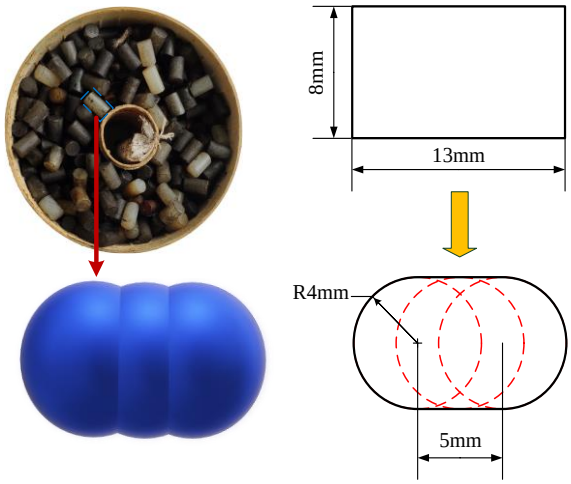

Fig. 1 Representations of cylindrical particles using multi-sphere method

500 mm. A combustible cartridge case holds a center core that is inserted into its center hole, which has a diameter of 30 mm. In this study, the Eulerian angle is used to define and illustrate the orientation of cylindrical particles due to their impact on simulation behavior. Figure 2(a) presents a schematic diagram depicting these angles, including the nutation angle (θ), precession angle (ψ), and spin angle (φ). Unlike conventional representations of Eulerian angles, the nutation angle in this study represents the angular difference between the long axis (X') of cylinder-shaped particles and that of the fixed system's X-axis, ranging from 0° to 180°.

3.3 Simulation Conditions

The Fluent software and EDEM software are connected on a single computer using coupling code to enable CFD and DEM simulations, where the CFD module tracks fluid phase information, and the DEM module tracks particle phase information. Each module operates as a particle factory, determining the precise locations of particles, with 770 particles contained within each modular container, resulting in 1540 particles within the system. The particles inside each modular cartridge in the simulation are uniformly colored red, green, yellow, and blue in the axial direction to observe their motion and distribution state, as illustrated in Fig. 2(b). The simulated particles were randomized across both modular containers regarding their orientation and position. All particles exhibit the same volume and density of 1500 kg/m^3, but have no initial velocity. Recovery coefficients of 0.5 were assigned for both inter-particle and wall-particle interactions, while the friction coefficients were respectively set at 0.25 and 0.35 for these groups. The k-ε model (Liu et al., 2020) or SST k-ω (Manda et al., 2021; Manda & Mazumdar, 2023b) model are commonly used in engineering practice to simulate turbulent gas flow. In this work, we employed the Realizable k-ε model available in ANSYS Fluent for precise simulation of turbulent flow, using a pressure-based solver and transient calculations to calculate the gas-particle flow. Gunpowder gas, which is characterized by high temperature and pressure, was modeled as ideal air with increasing temperature. The inlet boundary condition was set as a pressure inlet. It was expected that the modular cartridge would rupture, transitioning from a fixed boundary to an interface, as the pressure inside it exceeded 10 MPa. Notably, both modules ruptured sequentially from the primer end of the chamber towards the projectile base end.

4. RESULTS AND DISCUSSION

4.1 Experiments for Verifying Simulations

Verification of the experiments was carried out using a ballistic simulator configuration consisting of front plug, visualized chamber, external fixing bracket and rear plug. Chen and Yu (2022) designed an experimental apparatus for conducting cold-state experiments involving two modular charges within the cylinder chamber. This research establishes and verifies a three-dimensional unsteady gas-solid two-phase flow CFD-DEM model using particle accumulation data from investigations conducted by Chen and Yu (2022). The simulator chamber was constructed with a transparent tube of 135 mm in inside diameter and 13 mm in wall thickness. This design facilitated the visual observation of the movement and distribution of cylindrical particles when the modular cartridges ruptured. At one end of the tube, representing the base of the projectile, a nut mechanism with a control pressure diaphragm capable of withstanding pressures up to 46 MPa was used for closure. The other end represented

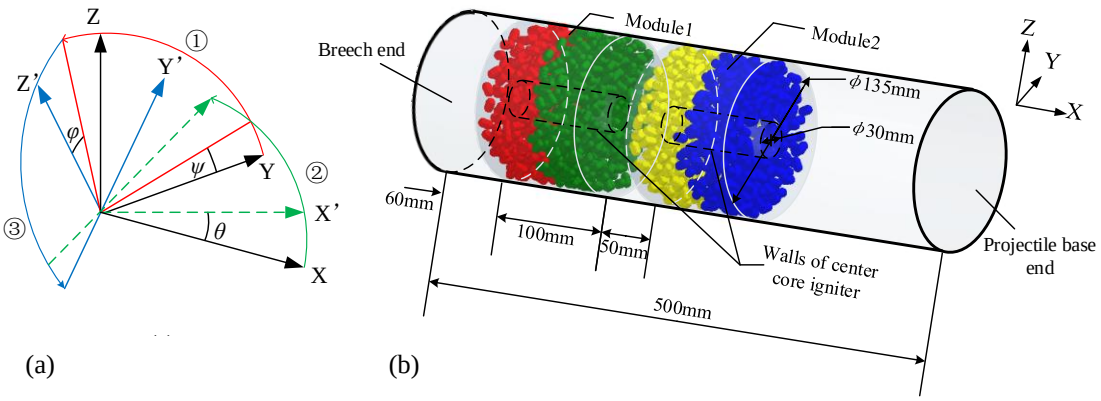

Fig. 2 Simulated propellant beds: (a) The schematic diagram of Euler angle, and x-y-z coordinate refers to fixed system; (b) The sketch map of the simulator chamber employed in this work

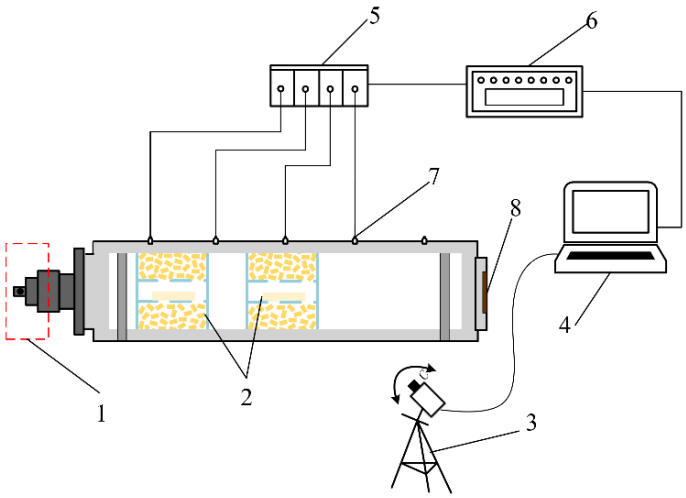

1.Firing mechanism 2. Modules 3.High-speed camera 4.Computer 5.Charge amplifier 6.Instantaneous state recorder 7.Pressure transducers 8.Control pressure diaphragm

Fig. 3 Schematic diagram of experimental device

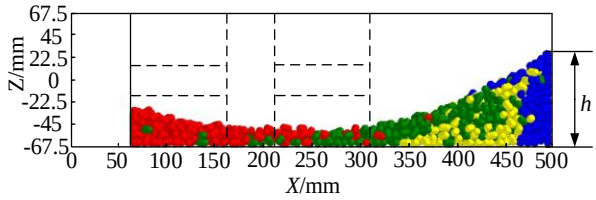

Fig. 4 Central X-Z cross-section of the final particle accumulation

the breech of the chamber and was equipped with a percussion primer. Additionally, the experimental platform included pressure transducers, data acquisition and processing equipment, as illustrated in Fig. 3.

The numerical simulation was conducted under experimental conditions, and Fig. 4 depicts an axial distribution of particle accumulation in the final state. The height of the final steep-slope accumulations (h) was measured at X-coordinate locations of 350, 400, 450, 475, and 500 mm, respectively, showing a high degree of consistency with the experimental results. To reduce the impact of grid resolution on simulation findings, three alternative grid resolutions were used to evaluate particle motion behavior and distribution following module cartridge rupture: 8316 (fine), 5404 (medium), and 2732 (coarse). The axial distribution of heights for steep-slope accumulations on the fine and coarse grid had the highest average relative error, 4.47%, and on the fine and medium grid, 2.42%, as shown in Fig. 5. No systematic differences were observed between the results calculated using the three grid configurations. To save computational time and reduce costs, the medium grid was ultimately chosen for all subsequent calculations. Figure 6 demonstrates that the error between the stacking height test and simulated measurement results remained within an acceptable range, emphasizing the high predictive accuracy of the CFD-DEM model established in the present investigation. Specifically, the model effectively captured gas-particle flow during the initial stages of interior ballistics when only partial ignition of propellant was observed.

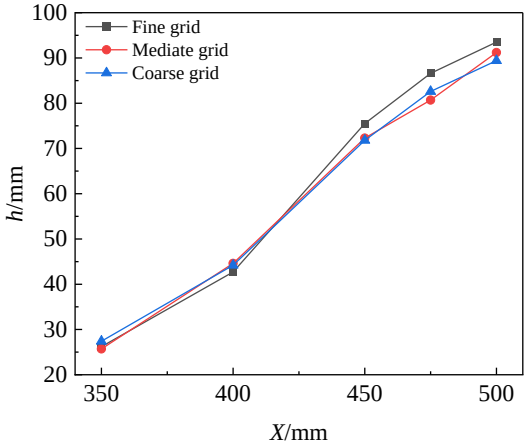

Fig. 5 Axial distribution of heights for steep-slope accumulations with different cell numbers

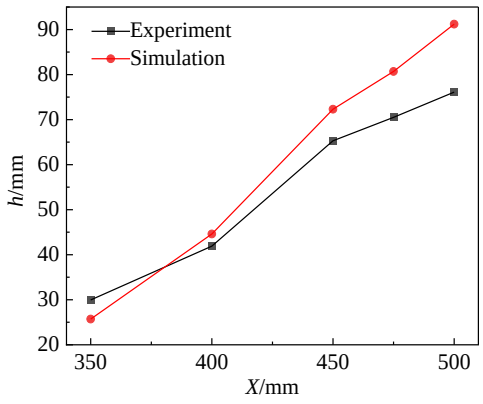

Fig. 6 Comparison between the simulations and the experiments: the stacking height distribution for the final particle accumulation

4.2 Characteristics of Gas-particle Flow

The initial process of the interior ballistics within the modular charge can be divided into the following stages: (1) The percussion primer is triggered, and its combustion products initiate the ignition of the igniter material

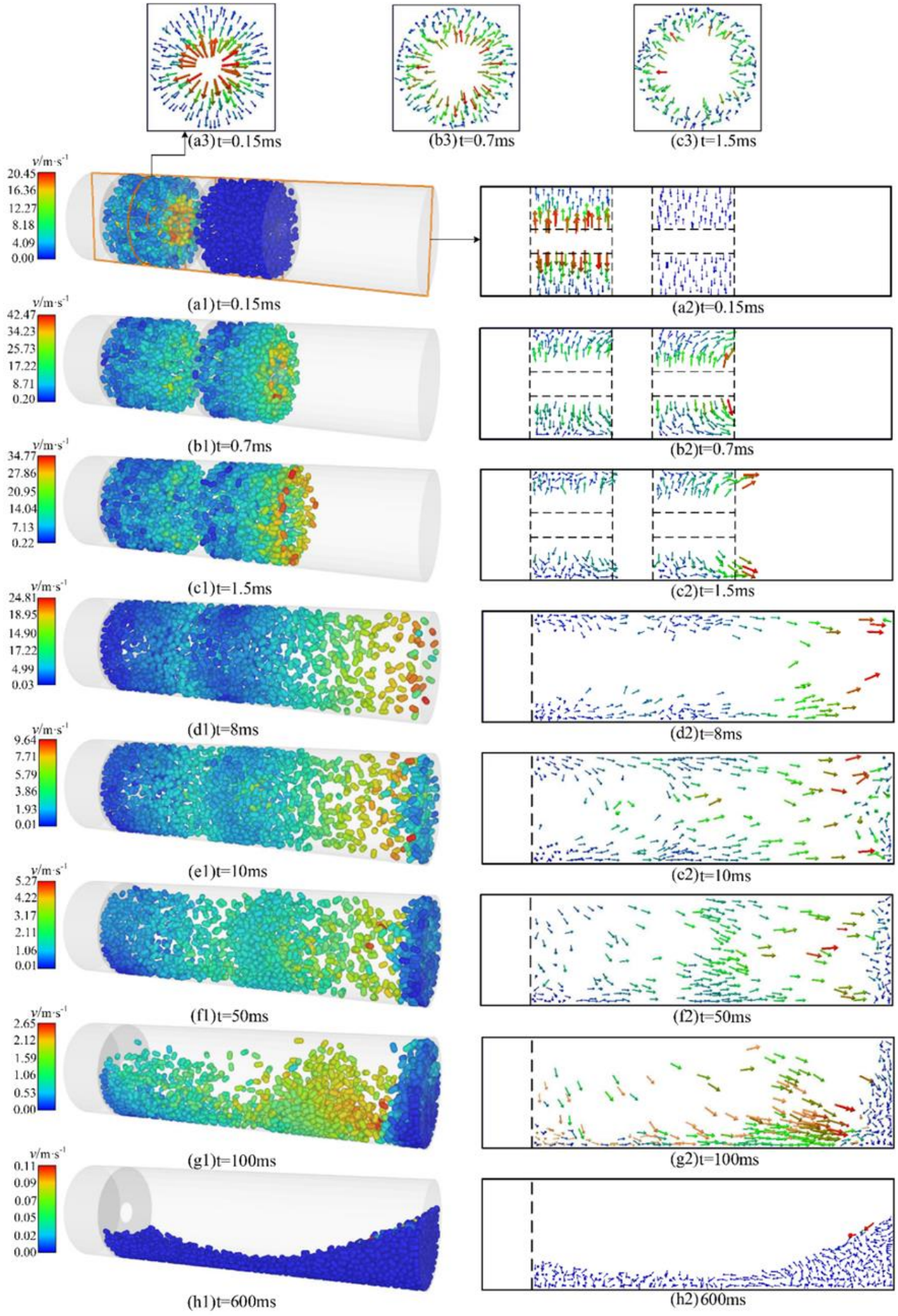

Fig. 7 Snapshots of particle flows colored by the particle velocity for the test condition

Table 1 Parameters of particle movement

Cases	*L*(mm)	Particle number	Maximum velocity(m/s^{-1})	Time(s)
A	30	1540	44.5	0.0090
B	60	1540	42.93	0.0077
C	90	1540	46.51	0.0068
D	120	1540	44.15	0.0056

attached to the center-core. (2) The actual granular propellants in the first module and near the center core are ignited using ignition gas. (3) As the solid propellants burn, they generate gases that increase the pressure within each module. (4) The walls of each module rupture due to differential pressure on opposite sides. (5) Non-spherical simulated particles are propelled by pressure gradients and interphase drag forces. The gunpowder gas is simplified to be equivalent to high-temperature and high-pressure gas flow, neglecting the flame propagation or heat transfer between the gas and chamber walls, for analysis of the gas-solid flow before and after rupture of the module cartridge. The particle accumulation formed during this period is considered the initial distribution of gunpowder particles for initiating complete combustion of the propellant. Indeed, the instantaneous particle velocity distributions at various times are illustrated in Fig. 7. An annular or tubular cluster of particles was formed in the module cartridge prior to module breakage, as seen in Fig. 7(a)–(c), where the particles were driven by radial high-pressure gas from the center core wall and extended radially towards the outer shell of the modular cartridge. Gunpowder gas acting on propellant grains will also cause the grains to undergo fluidization if the force is great enough, based on the fluidization properties of a spout-fluidized bed. However, due to the short duration of action for gunpowder gas, the phenomenon of fluidization in gunpowder particles was not clearly observed. Figure 7(b2) and (c2) demonstrate that when particles collided with the outer wall of the cartridge, they altered their direction of motion and continued moving to the right under the action of the pressure gradient. When no gas was transmitted to the simulator chamber, the particles ceased expanding radially, and there were also particles present in the center due to gravity. At 0.008 seconds, some particles moved toward the projectile base end and collided with the wall, resulting in particle velocity loss and reverse velocity, as shown in Fig. 7(d2) and (e2). Subsequently, as the simulation time progressed to 0.6 seconds, the number of actively moving particles decreased significantly. Specifically, less than 2% of the particles were observed to be in motion. This indicates that the solid distribution presented in Fig. 7(h1) and (h2) represents the final particle distribution.

4.3 The Influence of the Structure of Propellant Bed

The influence of the initial particle bed structure on particle accumulation characteristics was analyzed in this study by adjusting the position of modular containers. As shown in Table 1, only one parameter, denoted as *L* (the distance between Module 1 and the breech end), was varied while keeping a constant distance between Module 1 and Module 2. Numerical simulations were conducted

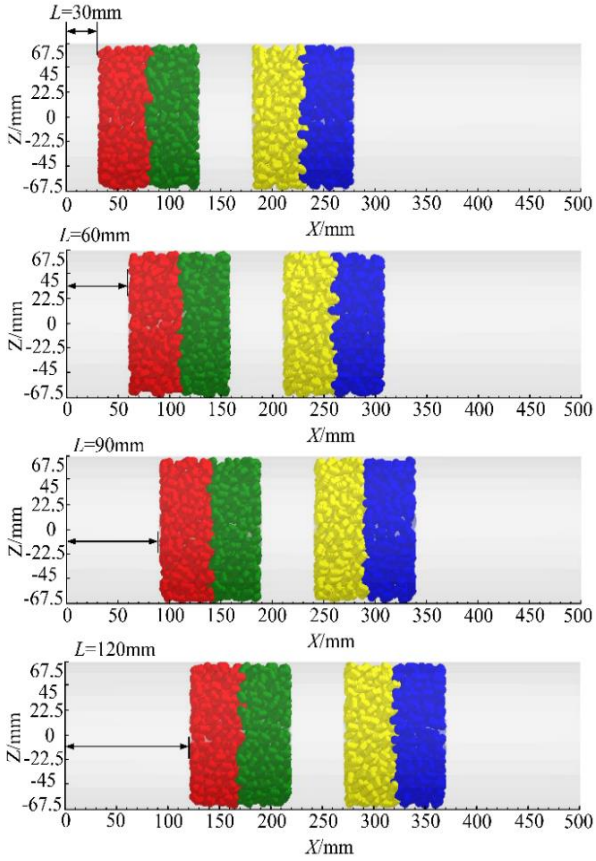

Fig. 8 Initial state of the various propellant beds for the different loading positions of the modules

on four cases, designated as case A to case D, with *L* values of 30, 60, 90, and 120 mm. Figure 8 illustrates the initial state of different particle bed structures. As the distance between Module 1 and the breech face increases, particles take less time to reach the projectile base wall decreases due to their unaffected velocity caused by the increase in *L* and the reduction in distance between the particles and the projectile base end of the chamber.

The maximum particle velocity of four different charge structures is illustrated in Fig. 9, showing a consistent trend in all cases. Initially, the maximum particle velocity experienced a rapid increase during the initial phase, followed by a zigzag decline after reaching its peak. The peak maximum velocity of particles is observed to occur between 0.7 and 0.9 milliseconds, with values ranging from 43 to 47 m/s. Figure 10 presents various typical particle distribution snapshots for different particle bed structures. At 4 milliseconds, particles underwent radial expansion and displayed rightward movement. Notably, the particles highlighted in green within Module 1 and those in blue within Module 2 exhibited higher velocities compared to other particles, resulting in a broader axial distribution within these modules. However, there was no intermixing observed between the two modules. Over time, the particles marked in blue on the right side of Module 2 gradually migrated towards and accumulated at the right wall of the chamber. Simultaneously, there was an increasing degree of

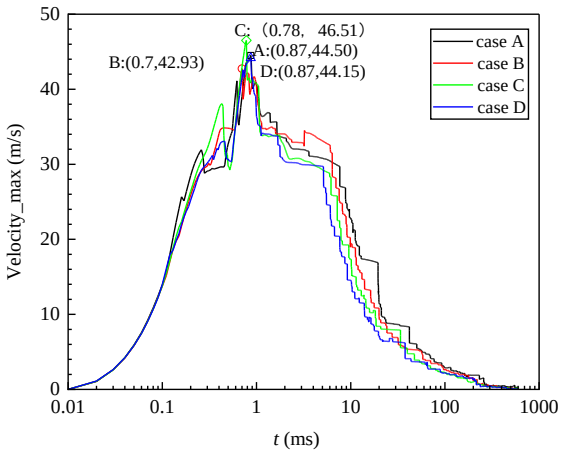

Fig. 9 Graph of the maximum velocity of particles with time for four cases

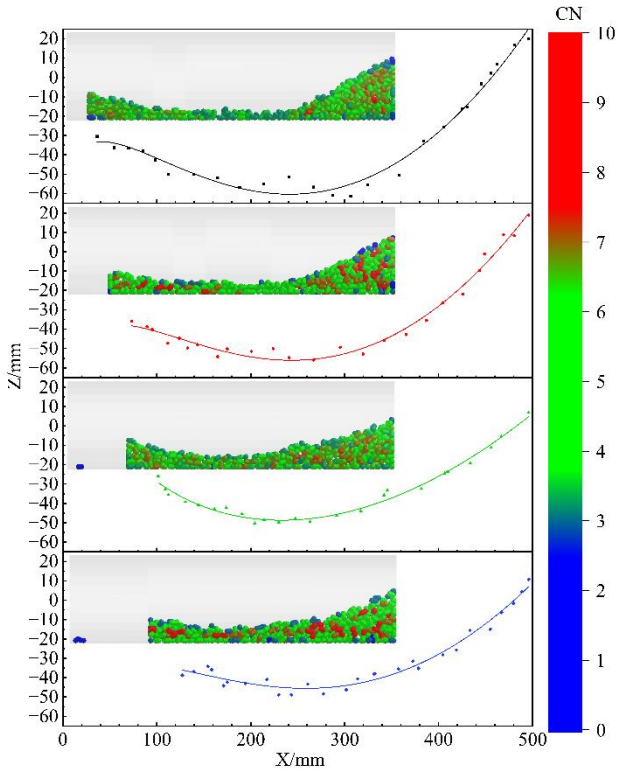

Fig. 10 distributions of particle coordination number for four cases

intermixing between neighboring particles in both modules, consisting of green and yellow-marked particles. The resulting particle distribution form exhibited a combination of gentle, horizontal, and steep slopes extending from the breech to the projectile base. Red-marked particles were primarily concentrated on the left side near the breech end with a gradual slope accumulation. A small number of red particles mixed with green particles to form a horizontally accumulated area on the left side. Green and yellow particles showed the highest degree of mixing and were mainly located in the lower part of steep-slope particle aggregation, whereas blue particles gathered in the upper half of steep-slope particle aggregation at the projectile base end. As shown in Fig. 10(a6) to (d6), the degree of particle mixing increased with an increase in L, resulting in a more even distribution of green and yellow-marked particles and a wider dispersion of red and blue-marked ones. Simulations indicate that when the pile reached a stable state, there were no significant protrusions or depressions on its surface. To characterize and quantify the shape of the particle packing, we extract the X and Z coordinates of the center-of-mass positions of particles in cross-sections along its central axis and fit them into a curve representing its height profile. It has been observed that this relationship between X and Z can be represented by a second-order polynomial function with the following specific expression:

$$Z = Ax^2 + Bx + C\sqrt{x} + D$$

$$\begin{cases} Z = 0.00165x^2 - 1.2651x + 14.5742\sqrt{x} - 77.45 \\ \qquad R^2 = 0.97729 \quad (L = 30) \\ Z = 0.00159x^2 - 1.3381x + 17.6576\sqrt{x} - 99.878 \\ \qquad R^2 = 0.98187 \quad (L = 60) \\ Z = 0.0004787x^2 + 0.1988x - 12.8094\sqrt{x} + 74.7386 \\ \qquad R^2 = 0.98141 \quad (L = 90) \\ Z = 0.00133x^2 - 1.2786x + 18.9298\sqrt{x} - 108.52 \\ \qquad R^2 = 0.97108 \quad (L = 120) \end{cases}$$

In order to reflect L's impact on particle packing form, the relationship between X, L, and Z is constructed. It is found that the equation of binary multiple terms is satisfied, and the expression is as follows:

$$Z = -24.26 + 0.3679X - 0.4013L - 0.00094XL - 0.00099X^2$$

Because the left end faces of modular cartridges were intact, there were minimal particles in the region where $X < L$. Therefore, we introduce an auxiliary parameter $Y = L - X > 0$ and reformulate the expression relating X, Y, and Z as follows:

$$\begin{aligned} Z &= -24.26 + 0.3679X - 0.4013\ (Y + X) \\ &\quad - 0.00094X(Y + X) + 0.00099X^2 \\ &= -24.26 - 0.0334X - 0.4013Y \\ &\quad - 0.00094XY + 0.00005X^2 \quad (Y > 0) \\ &\quad (R^2 = 0.9812) \end{aligned}$$

The total number of particles in the system that are in touch with a particle at any given time is represented by the coordination number (CN). Since particles in this work are constructed using the multi-sphere model, coordination number refers to the number of interactions a particle has with the spheres of other particles. Analyzing the distribution of CN provides a quantitative assessment of the contact status among particles within the propellant bed, which holds considerable significance for future investigations concerning particle combustion and heat transfer. More particles with high coordination numbers (CN), which indicate closer particle interactions and denser contact, were found inside the steep-slope particle aggregation, as illustrated in Fig. 11. In cases B and D, there were more particles with high CN present in

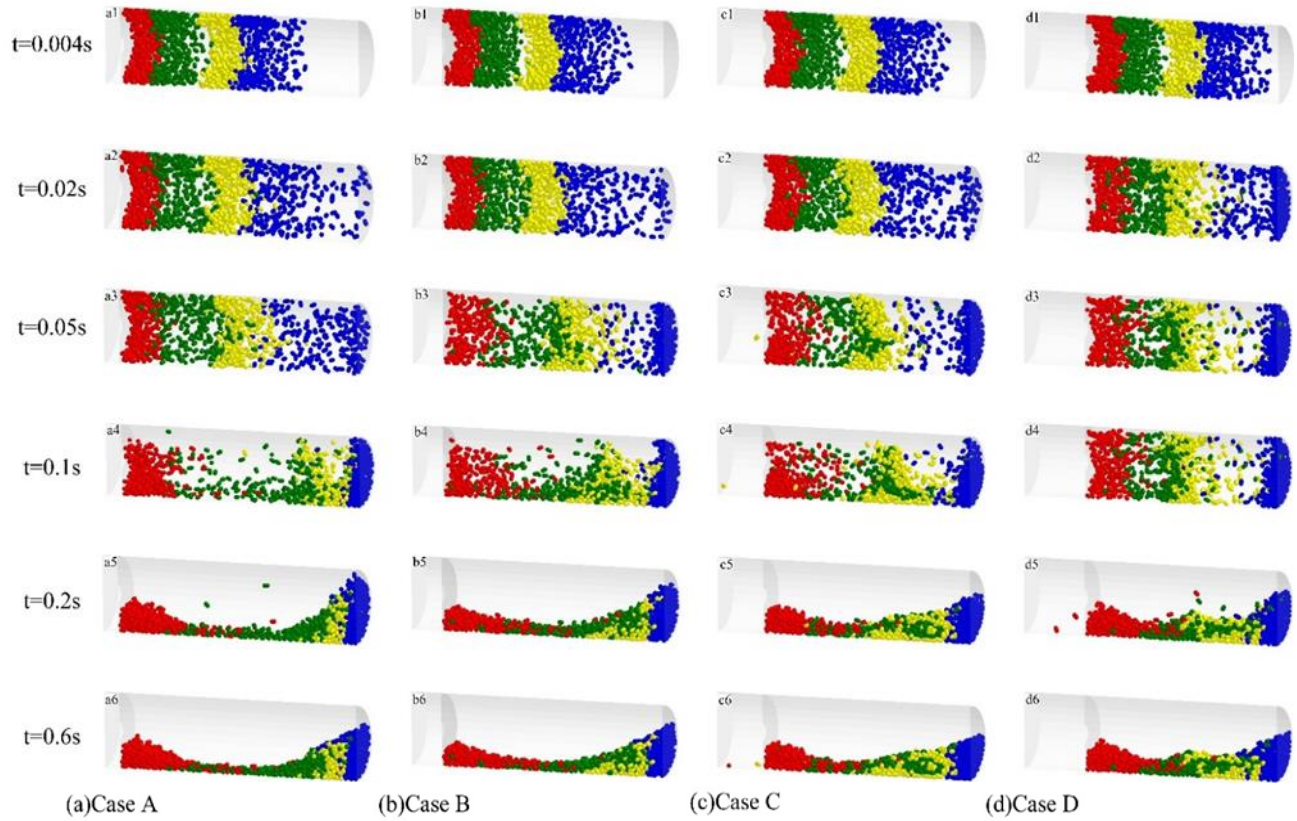

Fig. 11 Snapshots of the particle flows at different times for four cases

Table 2 Parameters of the final particle accumulation

Cases	L (mm)	L_h (mm)	α (°)	L_p (mm)
A	30	218.5	28.77	141.9
B	60	177.6	24.16	157.7
C	90	130.5	16.25	172.8
D	120	87.1	14.58	185.9

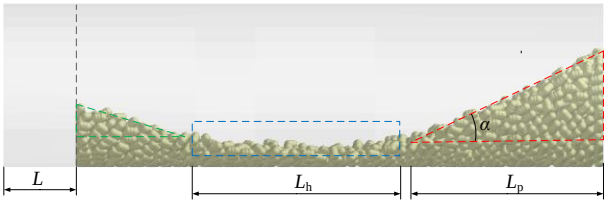

Fig. 12 Static accumulation of cylindrical particles at 600 milliseconds

the inner steep slope accumulation area, and a small number of particles with high CN were also found in the middle gentle slope and horizontal accumulation layers compared to cases A and C.

The distribution of particles at the base of the projectile was closely related to the generation of large-amplitude pressure waves, which significantly impacted launch accuracy and safety. To better understand particle distribution, the accumulation angle (α) and length (L_p) were used to characterize the shape of the steep-slope particle aggregation, as illustrated in Fig. 12. Based on the findings presented in Table 2, an increase in L resulted in a longer axial length for the steep slope while causing a decrease in its accumulation angle. This phenomenon can be attributed to the reduced distance between modules and the base wall as L increased, leading to a decrease in particle velocity loss. Consequently, more particles reached the end of the projectile base with higher velocities, leading to an increase in collisions with the base wall and a gain in reverse velocity. As a result, some particles acquired greater reverse velocity, facilitating smoother steep-slope accumulation on the projectile base end.

4.4 Particle Orientation

Particle orientation is a critical parameter for non-spherical particles, as it greatly affects the fluid flow resistance, the fluidization system's thermal characteristics, and the force that interacts between the particles and the fluid. Several researchers have examined how particle orientation varies in fluidized beds, with emphasis on the preferred orientation of particles near the wall (Oschmann et al., 2014). Figure 13 presents the particle orientation information at various times for different particle bed structures. The x-axis represents the particle orientation angle (θ), while the y-axis shows the count of particles with similar orientations within a 3° range ($\Delta\theta$ = 3°). Initially, because the orientation of particles filled in the modular cartridge case is randomly distributed, there is minimal variation in the number of particles with similar orientation angles ranging from 0 to 90°. However, the count of particles gradually decreased in the 90°-180° range. The orientation angle of particles stabilized over time, resulting in an inverted V-shaped distribution curve within the range of 0 to 180°. This

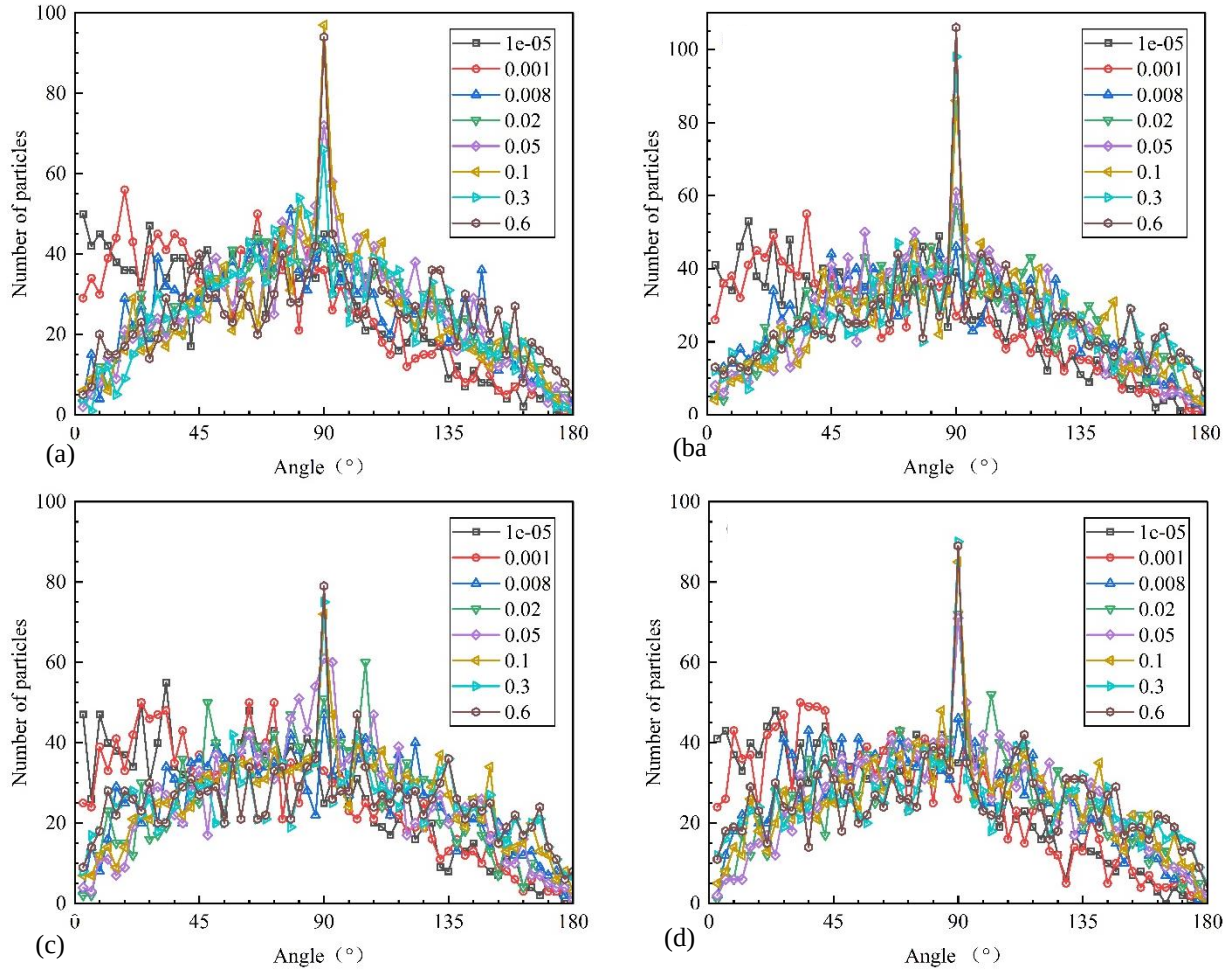

Fig. 13 Distribution of particle orientation angles at different times for (a) Case A, (b) Case B, (c) Case C, and (d) Case D

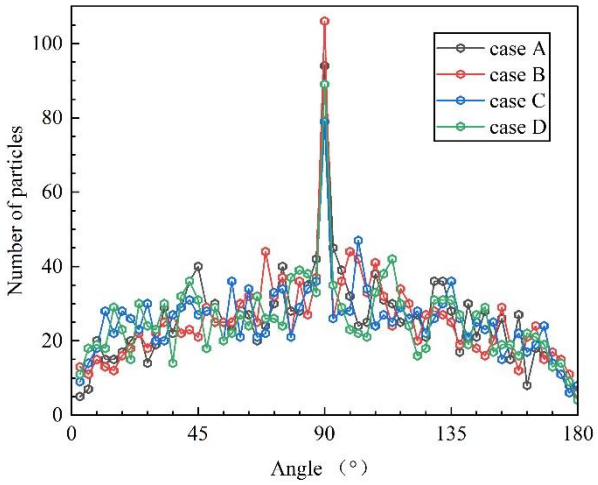

Fig. 14 Final distribution of particle orientation angles for four cases

observation suggested a prevalence of upright positions compared to other orientations, indicating a tendency for cylindrical particles to align their long axis perpendicular to the X-axis. Notably, the number of particles tending to be parallel to the X-axis significantly increased after 0.05 seconds, and this state persisted until reaching the final stable condition. Generally, particles tended to maintain a relatively stable horizontal position under gravity. However, due to the reverse force generated by the impact with the projectile base wall, the particles rotated and accumulated on a slope near the wall, leading to variations in particle orientation. As shown in Fig. 14, once particle distribution stabilized, particle orientation tended to be consistent across the four different initial particle bed structures, indicating that the overall distribution of particle orientation was not significantly affected by the loading position of the module. At 600 milliseconds, the propellant bed was considered a fixed bed. There were more particles with an orientation angle close to 90° in Cases A and B, while the total number of particles with an angle between the particle's long axis and the X-axis direction from 0 to 45° was lower compared to Cases C and D. No subsequent influence of module loading position was observed for particles with θ in the range of 90° to 180°.

5. CONCLUSION

CFD-DEM simulations were employed in the simulator chamber using the multi-sphere model to study

the spatial distribution and motion properties of cylindrical pellets. The impact of various module loading positions on particle packing structure and particle behavior was comprehensively examined. The modeling results, including particle accumulation height and shape, were found to be consistent with experimental data once the propellant bed achieved a stable state. The key findings are summarized as follows:

(a)When the particle distribution stabilizes, it exhibits a combination of gentle, horizontal, and steep slopes extending from the chamber's breech to the projectile base. The stacking height can be characterized by a second-order polynomial form. With Module 1 and Module 2 separated by a set distance of 40 mm, as the distance of Module 1 from the breech end increases, the angle of steep slope accumulation gradually decreases while the horizontal length L_p also increases, indicating a transition to a gentler slope.

(b)The initial loading positions of the modules consistently influenced both the system's particle coordination number distribution and maximum particle velocity. Particle maximum velocity exhibited rapid increases during the initial phase of movement, reaching a peak of approximately 43-47 m/s at 0.7-0.9 milliseconds, after which it gradually decreased. The majority of particles with high coordination numbers were observed to accumulate in the middle layer of steep slopes.

(c)Analysis of particle orientation revealed that, following collision with the right projectile base wall, the number of particles displayed an inverted V-shape within the orientation angle range of 0° to 180°, indicating that the majority of particles align themselves vertically, with 90° being their preferred orientation angle, while the number of particles oriented horizontally decreased.

ACKNOWLEDGEMENTS

The authors are grateful for the financial support of the National Natural Science Foundation of China. (Grand No. 52076111)

CONFLICT OF INTEREST

The authors declare that they have no known competing financial interests or personal relationships that could have appeared to influence the work reported in this paper.

AUTHORS CONTRIBUTION

Z. Y. Li: Writing-Original draft preparation, Conceptualization, Software, Validation. **Y. G. Yu**: Visualization, Supervision, Writing-Reviewing and Editing. **A. Chen**: Methodology.

REFERENCES

Atxutegi, A., Kieckhefen, P., Pietsch, S., Aguado, R., Olazar, M., & Heinrich, S. (2021). Unresolved CFD-DEM simulation of spherical and ellipsoidal particles in conical and prismatic spouted beds. *Powder Technology*, *389*, 493-506. https://doi.org/10.1016/j.powtec.2021.05.012

Briand, M. R., Tissier, M. P. Y., & Reynaud, M. C. (1992, 1-3 June). *Theoretical modeling of ballistics processes of modular charges for large caliber guns*. 13th International Symposium on Ballistics, Stockholm, Sweden.

Chen, A., & Yu, Y. (2022). CFD-DEM simulation on the complex gas-solid flow in a closed chamber with particle groups. *Journal of Mechanical Science and Technology*, *36*(11), 5523-5535. https://doi.org/10.1007/s12206-022-1017-6

Chen, A., & Yu, Y. (2023). Investigation of particle distribution after the energetic module broken in the ignition process of gun. *Case Studies in Thermal Engineering*, *41*, 102619. https://doi.org/10.1016/j.csite.2022.102619

Chen, L., Sun, Z., Ma, H., Pan, G., Li, P., & Gao, K. (2022). Flow characteristics of pneumatic conveying of stiff shotcrete based on CFD-DEM method. *Powder Technology*, *397*, 117109. https://doi.org/10.1016/j.powtec.2022.117109

Cheng, C., & Zhang, X. (2013). Modeling of interior ballistic gas-solid flow using a coupled computational fluid dynamics-discrete element method. *Journal of Applied Mechanics*, *80*(3), 314031-314036. https://doi.org/10.1115/1.4023313

Cundall, P. A., & Strack, O. D. L. (1979). A discrete numerical model for granular assemblies. *Géotechnique*, *1*(29), 47-65. https://doi.org/10.1680/geot.1979.29.1.47

Gao, X., Yu, J., Portal, R. J., Dietiker, J. F., Shahnam, M.,& Rogers, W. A. (2022). Development and validation of SuperDEM for non-spherical particulate systems using a superquadric particle method. Particuology, 61, 74-90. https://doi.org/10.1016/j.partic.2020.11.007

Haider, A., & Levenspiel, O. (1989). Drag coefficient and terminal velocity of spherical and nonspherical particles. *Powder Technology*, *58*(1), 63-70. https://doi.org/10.1016/0032-5910(89)80008-7

Hertz H. (1882) Über die Berührung fester elastischer Körper (On the contact of elastic solids). *Journal fur die Reine und Angewandte Mathematik*, *92*, 156-171. https://doi.org/10.1515/crll.1882.92.156

Höhner, D., Wirtz, S., & Scherer, V. (2012). A numerical study on the influence of particle shape on hopper discharge within the polyhedral and multi-sphere discrete element method. *Powder Technology*, *226*, 16-28. https://doi.org/10.1016/j.powtec.2012.03.041

Lei, X., Liao, Y., Zhang, Q., Wang, L., & Liao, Q. (2018). Numerical simulation of seed motion characteristics of distribution head for rapeseed and wheat. *Computers and Electronics in Agriculture*, *150*, 98-109. https://doi.org/10.1016/j.compag.2018.04.009

Li, S., Zhao, P., Xu, J., Zhang, L., & Wang, J. (2022). CFD-DEM simulation of polydisperse gas-solid flow

of Geldart A particles in bubbling micro-fluidized beds. *Chemical Engineering Science*, *253*, 117551. https://doi.org/10.1016/j.ces.2022.117551

Liu, X., Gan, J., Zhong, W., & Yu, A. (2020). Particle shape effects on dynamic behaviors in a spouted bed: CFD-DEM study. *Powder Technology*, *361*, 349-362. https://doi.org/10.1016/j.powtec.2019.07.099

Liu, X., Zhong, W., Jiang, X., & Jin, B. (2015). Spouting behaviors of binary mixtures of cylindroid and spherical particles. *AIChE Journal*, *61*(1), 58-67. https://doi.org/10.1002/aic.14636

Lu, Z., Zhou, Y., & Wang, Y. (1999). Two phase flow interior ballistic simulation of the short-barrel gun with modular charges. *Journal of Nanjing University of Science and Technology*, *23*(2), 105-108. https://doi.org/10.3969/j.issn.10059830.1999.02.003

Lu, Z., & Zhou, Y. (1999). Two-phase-combustion model and numerical simulation of pressure wave in the gun with modular charges. *Explosion and Shock Waves*, *19*(3), 269-273. https://doi.org/10.3321/j.issn:1001-1455.1999.03.013

Lu, Z., & Zhou, Y. (2001). Two-dimensional two-phase flow numerical simulation of interior ballistic processes in a gun with modular charges. *Acta Armamentarii*, *22*(3), 298-301. https://doi.org/10.3321/j.issn:1000-1093.2001.03.003

Ma, H., & Zhao, Y. (2018a). CFD-DEM investigation of the fluidization of binary mixtures containing rod-like particles and spherical particles in a fluidized bed. *Powder Technology*, *336*, 533-545. https://doi.org/10.1016/j.powtec.2018.06.034

Ma, H., & Zhao, Y. (2018b). Investigating the flow of rod-like particles in a horizontal rotating drum using DEM simulation. *Granular Matter*, *20*, 1-15. https://doi.org/10.1007/s10035-018-0823-0

Manda, U., & Mazumdar, S. (2023a). Effects of buoyancy in a horizontal microchannel in a laminar flow of supercritical carbon dioxide (sCO_2) at different gravities. *SSRN*. http://dx.doi.org/10.2139/ssrn.4591011

Manda, U., & Mazumdar, S. (2023b). Effect of cross-sectional shape on flow and heat transfer characteristics of the laminar flow of supercritical carbon dioxide (sCO_2) inside horizontal microchannels. *SSRN*. http://dx.doi.org/10.2139/ssrn.4596518

Manda, U., Parahovnik, A., & Peles, Y. (2020). *Theoretical investigation of boundary layer behavior and heat transfer of supercritical carbon dioxide (sCO_2) in a Microchannel.* 19th IEEE Intersociety Conference on Thermal and Thermomechanical Phenomena in Electronic Systems (ITherm), Orlando, FL, USA. http://doi.org/10.1109/ITherm45881.2020.9190408

Manda, U., Parahovnik, A., & Peles, Y. (2022). Thermoacoustic waves and piston effect inside a microchannel with carbon dioxide near critical conditions. *Thermal Science and Engineering Progress*, *36*, 101528. https://doi.org/10.1016/j.tsep.2022.101528

Manda, U., Parahovnik, A., Mazumdar, S., & Peles, Y. (2023). Heat transfer characteristics of turbulent flow of supercritical carbon dioxide (sCO_2) in a short-heated microchannel. *International Journal of Thermal Sciences*, *192*, 108389. https://doi.org/10.1016/j.ijthermalsci.2023.108389

Manda, U., Peles, Y., & Putnam, S. (2021). *Comparison of heat transfer characteristics of flow of supercritical carbon dioxide and water inside a square microchannel.* 20th IEEE Intersociety Conference on Thermal and Thermomechanical Phenomena in Electronic Systems (iTherm), San Diego, CA, USA. http://doi.org/10.1109/ITherm51669.2021.9503192

Mindlin, R. D. (1949). Compliance of elastic bodies in contact. *Journal of Applied Mechanics*, *16*, 259-268. https://doi.org/10.1115/1.4009973

Mindlin, R. D. & Deresiewicz, H. (1953). Elastic spheres in contact under varying oblique force. *ASME, Journal of Applied Mechanics*, *20*, 327-344. https://doi.org/10.1115/1.4010702

Nan, W., Wang, Y., Ge, Y., & Wang, J. (2014). Effect of shape parameters of fiber on the packing structure. *Powder Technology*, *261*, 210-218. https://doi.org/10.1016/j.powtec.2014.04.048

Norouzi, H. R., Zarghami, R., Sotudeh-Gharebagh, R., & Mostoufi, N. (2016). *Coupled CFD-DEM modeling: formulation, implementation and application to multiphase flows*. John Wiley & Sons.

Oschmann, T., Hold, J., & Kruggel-Emden, H. (2014). Numerical investigation of mixing and orientation of non-spherical particles in a model type fluidized bed. *Powder Technology*, *258*, 304-323. https://doi.org/10.1016/j.powtec.2014.03.046

Oschmann, T., Vollmari, K., Kruggel-Emden, H., & Wirtz, S. (2015). Numerical investigation of the mixing of non-spherical particles in fluidized beds and during pneumatic conveying. *Procedia Engineering*, *102*, 976-985. https://doi.org/10.1016/j.proeng.2015.01.220

Ren, B., Zhong, W., Jiang, X., Jin, B., & Yuan, Z. (2014). Numerical simulation of spouting of cylindroid particles in a spouted bed. *The Canadian Journal of Chemical Engineering*, *92*(5), 928-934. https://doi.org/10.1002/cjce.21900

Shao, Y., Zhong, W., Chen, X., Chen, Y., & Jin, B. (2014). Spouting of non-spherical particles in conical-cylindrical spouted bed. *The Canadian Journal of Chemical Engineering*, *92*(4), 742-746. https://doi.org/10.1002/cjce.21888

Sheu, T. W. H., & Lee, S. M. (1995). Analysis of combustion processes in a gun interior ballistics. *International Journal of Computational Fluid*

Dynamics, 4(1-2), 57-71. https://doi.org/10.1080/10618569508904518

Soltanbeigi, B., Podlozhnyuk, A., Papanicolopulos, S. A., Kloss, C., Pirker, S., & Ooi, J. Y. (2018). DEM study of mechanical characteristics of multi-spherical and superquadric particles at micro and macro scales. Powder Technology, 329, 288-303. https://doi.org/10.1016/j.powtec.2018.01.082

Tao, H., Jin, B., Zhong, W., Wang, X., Ren, B., Zhang, Y., & Xiao, R. (2010). Discrete element method modeling of non-spherical granular flow in rectangular hopper. *Chemical Engineering and Processing: Process Intensification*, *49*(2), 151-158. https://doi.org/10.1016/j.cep.2010.01.006

Tsuji, Y., Tanaka, T., & Ishida, T. (1992). Lagrangian numerical simulation of plug flow of cohesionless particles in a horizontal pipe. *Powder Technology*, *71*(3), 239-250. https://doi.org/10.1016/0032-5910(92)88030-L

Wang, T., Gao, Q., Deng, A., Tang, T., & He, Y. (2021). Numerical and experimental investigations of instability in a spouted bed with non-spherical particles. *Powder Technology*, *379*, 231-240. https://doi.org/10.1016/j.powtec.2020.10.032

Wang, T., He, Y., Tang, T., & Zhao, Y. (2016). Numerical investigation on particle behavior in a bubbling fluidized bed with non-spherical particles using discrete hard sphere method. *Powder Technology*, *301*, 927-939. https://doi.org/10.1016/j.powtec.2016.07.005

Wei, G., Zhang, H., An, X., Xiong, B., & Jiang, S. (2019). CFD-DEM study on heat transfer characteristics and microstructure of the blast furnace raceway with ellipsoidal particles. *Powder Technology*, *346*, 350-362. https://doi.org/10.1016/j.powtec.2019.02.022

Zhao, H., An, X., Gou, D., Zhao, B., & Yang, R. (2018). Attenuation of pressure dips underneath piles of spherocylinders. *Soft Matter*, *14*(21), 4404-4410. https://doi.org/10.1039/C8SM00280K

Zhao, Y. (2003). Numerical simulation for ignition and flame-spreading of modular charge. *Chinese Journal of Explosives & Propellants*, *26*(2), 32-35. https://doi.org/10.3969/j.issn.10077812.2003.02.012

Zhang, X. & Yuan, Y. (2016). *Theories and applications of multiphase flow dynamics in high temperature and high pressure*. Beijing Institute of Technology Press.

Zhou, L., Lv, W., Bai, L., Han, Y., Wang, J., Shi, W., & Huang, G. (2022). CFD-DEM study of gas-solid flow characteristics in a fluidized bed with different diameter of coarse particles. *Energy Reports*, *8*, 2376-2388. https://doi.org/10.1016/j.egyr.2022.01.174